Regular Article

Online Three-Axis Magnetometer Hard-Iron and Soft-Iron Bias and Angular Velocity Sensor Bias Estimation Using Angular Velocity Sensors for Improved Dynamic Heading Accuracy

Andrew R. Spielvogel^{1,2}, Abhimanyu S. Shah¹ and Louis L. Whitcomb¹ and Louis L. Whitcomb¹ and Louis L. Whitcomb¹ Abhimanyu S. Shah¹ and Louis L. Whitcomb¹ and Louis

Abstract: This article addresses the problem of dynamic online estimation and compensation of hard-iron and soft-iron biases of three-axis magnetometers under dynamic motion in field robotics, utilizing only biased measurements from a three-axis magnetometer and a three-axis angular rate sensor. The proposed magnetometer and angular velocity bias estimator (MAVBE) utilizes a 15-state process model encoding the nonlinear process dynamics for the magnetometer signal subject to angular velocity excursions, while simultaneously estimating nine magnetometer bias parameters and three angular rate sensor bias parameters, within an extended Kalman filter framework. Bias parameter local observability is numerically evaluated. The bias-compensated signals, together with three-axis accelerometer signals, are utilized to estimate bias-compensated magnetic geodetic heading. Performance of the proposed MAVBE method is evaluated in comparison to the widely cited magnetometer-only TWOSTEP method in numerical simulations, laboratory experiments, and full-scale field trials of an instrumented autonomous underwater vehicle in the Chesapeake Bay, Maryland, USA. For the proposed MAVBE, (i) instrument attitude is not required to estimate biases, and the results show that (ii) the biases are locally observable, (iii) the bias estimates converge rapidly to true bias parameters, (iv) only modest instrument excitation is required for bias estimate convergence, and (v) compensation for magnetometer hard-iron and soft-iron biases dramatically improves dynamic heading estimation accuracy.

Keywords: magnetometer hard-iron bias and soft-iron bias calibration, angular velocity sensor bias calibration, navigation, field robotics, GPS-denied navigation

Received: 16 January 2021; revised: 28 May 2021; accepted: 2 August 2021; published: 31 May 2022.

Correspondence: Louis L. Whitcomb, Johns Hopkins University, Department of Mechanical Engineering, Baltimore, MD, USA, Email: Ilw@jhu.edu

This is an open-access article distributed under the terms of the Creative Commons Attribution License, which permits unrestricted use, distribution, and reproduction in any medium, provided the original work is properly cited.

Copyright © 2022 Spielvogel, Shah and Whitcomb

DOI: https://doi.org/10.55417/fr.2022033

1. Introduction

The dynamic instrumentation and estimation of vehicle attitude, especially geodetic heading, is critical to accurate navigation of land, sea, and air vehicles in dynamic motion. The utility of the ubiquitous nine-axis inertial measurement unit (IMU) (with three-axis magnetometers, three-axis angular rate sensors, and three-axis accelerometers) for accurate heading estimation is commonly vitiated by very significant hard-iron and soft-iron magnetometer biases, as well as by angular-rate sensor biases. Many previously reported bias estimation approaches are complicated by (i) the need to know the instrument's real-time attitude (heading, pitch, and roll) or (ii) the need for the instrument to experience very large attitude motion excursions (which may be infeasible for instruments mounted in many full-scale vehicles).

This article reports a novel method for dynamic online estimation of hard-iron and soft-iron biases of three-axis magnetometers under dynamic motion (rotation and translation) without any knowledge of the instrument's real-time attitude. Our approach is to formulate a nonlinear process dynamics model for the variation in the magnetic field vector over time as the instrument is subject to a priori unknown angular velocities. We report a 15-state bias estimator utilizing this process model that simultaneously estimates (i) a three-axis dynamic process-model estimate of the true magnetic field vector, (ii) all six soft-iron bias magnetometer bias terms, (iii) all three hard-iron bias magnetometer bias terms, and (iv) all three angular velocity sensor bias terms. The proposed magnetometer and angular velocity bias estimator (MAVBE) is implemented as an extended Kalman filter (EKF) in which the difference between the estimated process model magnetometer measurement and the actual observed magnetometer measurement provide the EKF innovations. The three-axis accelerometer signal is then utilized with the estimator signals to provide improved-accuracy gyro-stabilized dynamic heading estimation. Note that the present study does not address accelerometer bias estimation, which has been addressed in previously reported studies (e.g., Batista et al., 2011; Troni and Whitcomb, 2019).

The present study reports a performance analysis and comparison to the widely cited magnetometer-only TWOSTEP method (Alonso and Shuster, 2002b). The reported MAVBE is compared to the TWOSTEP method in a numerical simulation study, in full-scale laboratory experimental trials with a nine-axis IMU on the Johns Hopkins University (JHU) remotely operated vehicle (ROV), Figure 1, and in at-sea field experimental trials with a nine-axis IMU on the JHU Iver3 autonomous underwater vehicle (AUV) in the Chesapeake Bay, Maryland, USA, Figure 2.

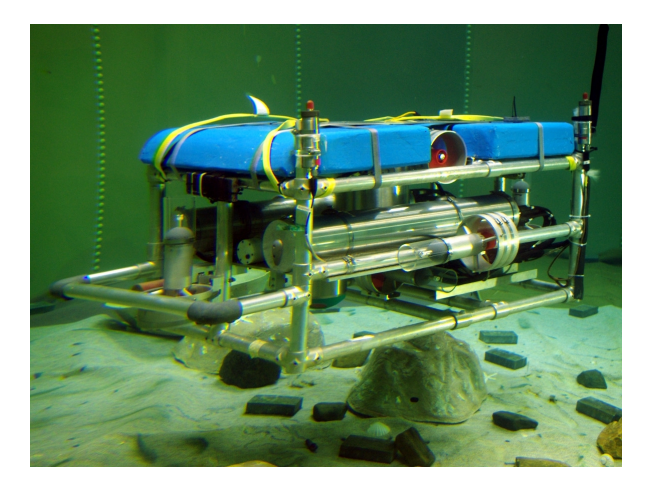


Figure 1. Full-scale experimental trials were conducted with the Johns Hopkins University (JHU) remotely operated vehicle (ROV) in a laboratory test tank (diameter of 7.5 m and height of 4 m). The JHU ROV has a full suite of navigation sensors, including several inertial measurement units (IMUs), typically found on deep submergence underwater vehicles.



Figure 2. Field trials were conducted with the Johns Hopkins University (JHU) Iver3 autonomous underwater vehicle (AUV) in the Chesapeake Bay, Maryland, USA (OceanServer Technology, Inc., 2016). The JHU Iver3 has a full suite of navigation sensors, including a Doppler velocity log (DVL) and several IMUs (Image credit: Paul Stankiewicz, JHU).

Advantages of the proposed MAVBE approach include the following: (i) knowledge of the instrument attitude is not required for sensor bias estimation, (ii) the system is shown numerically to be locally observable, (iii) bias estimates converge rapidly to true bias parameters, (iv) only modest instrument excitation is required for bias estimate convergence, and (v) magnetometer hard-iron and soft-iron bias compensation is shown to dramatically improve dynamic heading estimation accuracy.

1.1. Background and Motivation

Accurate sensing and estimation of attitude (i.e. geodetic heading, and roll and pitch referenced to the local gravitational field) are critical components of navigation systems for a wide variety of robotic vehicles. The need for accurate attitude estimation is particularly acute in the case of vehicles operating in global positioning system (GPS)-denied environments such as underwater.

The development of a new generation of small low-cost underwater vehicles (UVs) has begun to enable oceanographic, environmental assessment and national security missions that were previously considered impractical or infeasible (Clegg and Peterson, 2003; Clem et al., 2012; Corke et al., 2007; Dunbabin et al., 2005; Packard et al., 2013; Steele et al., 2012; Zhou et al., 2014). These small low-cost robotic vehicles commonly employ microelectromechanical systems (MEMS) IMUs comprised of three-axis MEMS magnetometers, angular rate sensors, and accelerometers to estimate local magnetic heading, pitch, and roll, typically to within several degrees of accuracy, but require careful soft-iron and hard-iron calibration and compensation to achieve these accuracies (Crassidis et al., 2007; Guo et al., 2008; Hamel and Mahony, 2006; Mahony et al., 2008, 2012; Metni et al., 2005, 2006; Wu et al., 2015). Moreover, magnetic attitude sensors must be recalibrated for soft-iron and hard-iron biases whenever the vehicle's physical configuration changes significantly (i.e., sensors or other payloads added or removed), as very commonly occurs on oceanographic marine vehicles. Studies have shown that the accuracy of magnetic heading sensors is often the principal error source in overall navigation solutions (Kinsey and Whitcomb, 2004). In addition, EKFs rely on the assumption that noise is zero-mean Gaussian. The addition of uncompensated sensor biases introduces nonzero-mean noise that corrupts the accuracy of navigation EKFs (Barfoot, 2017). Thus it is essential to estimate accurately and compensate for attitude sensor biases in order to achieve high-accuracy attitude estimation. However, most previously reported approaches for hard-iron and soft-iron bias calibration require significant angular motion of the instrument in all three degrees of freedom (roll, pitch, heading), which can be impractical or infeasible on many UVs and land vehicles that are passively stable in roll and pitch. These vehicles may be unable to achieve the large roll and pitch rotations needed for traditional magnetometer calibration methods. We show that the use of angular-rate signals in the proposed MAVBE method enables the calibration to be performed with small vehicle changes in roll and pitch, thus enabling the calibration of land and underwater vehicle compasses.

1.2. Literature Review

The present study addresses the problem of IMU sensor bias estimation and attitude estimation utilizing only the signals from the IMU itself. This study does not address the different problem of achieving IMU sensor bias estimation/compensation and full-state and attitude estimation with multisensor fusion of IMUs in combination with additional external sensors, which has been addressed in previous studies, for example for IMU+GPS (e.g. Vasconcelos et al., 2011), IMU+computer vision (e.g., Scaramuzza et al., 2014), and IMU+Lidar (e.g., Bry et al., 2012). The motivation for the current study's focus on IMU sensor bias estimation utilizing only signals from the IMU is that many field robots, e.g., fully submerged UVs, generally do not have access to additional external sensor signals such as from GPS, cameras, or lidar.

Previously reported methods for estimating magnetometer hard-iron biases only have been reported by Wu (2019) and Fedele et al. (2018), but they do not address the estimation of soft-iron magnetometer bias. The estimation of hard-iron bias only differs from the problem solved by the present paper which addresses both hard-iron and soft-iron bias estimation.

Many batch methods for magnetometer estimation are reported in the literature. Geophysics researchers commonly use batch methods for magnetometer calibration (Bronner et al., 2013; Honsho et al., 2013). Zhu et al. (2019) formulate the calibration as a least-squares problem and required the integration of angular rates over time to create a rotation matrix that is used to rotate signals back to the initial instrument frame. This integration, however, introduces random walk errors which grow with time. In consequence, this approach can only provide coarse magnetometer calibration; it cannot provide fine magnetometer calibration. This limitation is noted by the authors, where they observe that the resulting magnetometer calibration "can serve as a coarse calibration method alone or be used as a good initial value for other fine algorithms for more accurate result" (Zhu et al., 2019).

Alonso and Shuster (2002a) propose the TWOSTEP method for estimating magnetometer sensor bias, and an extended method (Alonso and Shuster, 2002b) for calculating magnetometer scale and orthogonality factors as well. Vasconcelos et al. (2011) report magnetometer bias estimation as an ellipsoid fitting problem which can be solved with an iterative maximum likelihood estimate approach. Many least-squares methods are reported for the ellipsoid fitting problem (Ammann et al., 2015; Dinale, 2013; Fang et al., 2011; Foster and Elkaim, 2008; Ousaloo et al., 2017) and Wu et al. (2013) frame the ellipsoid fitting problem as a particle swarm optimization. Kok et al. (2012) and Li and Li (2012) fuse accelerometer measurements with magnetometer measurements to estimate magnetometer sensor bias, and Papafotis and Sotiriadis (2019) report an algorithm for three-axis accelerometer and magnetometer calibration using a gradient descent method. All of these methods, however, require large angular rotations of the instrument to achieve accurate bias estimation (which is infeasible for instruments mounted in many full-scale vehicles) and, moreover, they are batch estimators that are not designed for online estimation of magnetometer sensor bias.

Sensor biases change over time due to changes in the configuration and payloads of the host vehicle, temperature, etc., which make it imperative to estimate sensor biases in real time. Troni and Whitcomb (2019) report a novel method utilizing angular velocity measurements for estimating magnetometer hard-iron sensor biases, but this approach does not address soft-iron calibration and it assumes that the angular velocity sensor signal is already bias compensated. Spielvogel and Whitcomb (2018a) extended the work by Troni and Whitcomb (2019) to include estimation of

angular-rate gyroscope and accelerometer measurement biases, but this approach again does not address soft-iron magnetometer bias calibration.

Spielvogel and Whitcomb (2020) report an adaptive observer for magnetometer hard-iron and soft-iron biases in two-axis magnetometers. However, this observer does not provide the full calibration of three-axis magnetometers and is only suitable for robotic vehicles which experience small roll and pitch rotations.

Crassidis et al. (2005) report an extension to Alonso and Shuster's TWOSTEP method (Alonso and Shuster, 2002b,a), based on the EKF. Guo et al. (2008) report an alternative EKF approach for doing magnetometer sensor bias estimation. However, these approaches require large angular rotations of the instrument for accurate magnetometer calibration, similar to the batch methods mentioned above.

Soken and Sakai (2019) report a magnetometer calibration method using the TRIAD algorithm and an unscented Kalman filter (UKF). However, this method requires knowledge of the initial attitude of the instrument and exhibits a lengthy convergence time.

Han et al. (2017) report a gyroscope-aided EKF method for magnetic calibration. However, based upon our review of source code kindly provided by the original authors, this approach appears to integrate the angular rate forward in time, which introduces random walk; thus it is not clear that it can be used continuously for a long period of time. In addition, their algorithm requires large angular rates for the hard-iron bias to converge and appears to be unable to identify the hard- or soft-iron biases of high-end MEMS IMUs like the ones used in the current paper.

The study by Wu et al. (2018) reports an error-state EKF for estimating nine-degree-of-freedom IMU sensor biases including the hard- and soft-iron biases of a magnetometer, and sensor rotation between the magnetometer sensor and the "inertial sensors" (which are the accelerometer and angular rate sensor). This approach, an error-state EKF, differs from the full-state EKF reported in our study.

Previous studies by the present authors on IMU bias estimation differs from the present article in the following ways:

- Two papers by Spielvogel and Whitcomb (2018b, 2019) do not address magnetometer calibration and instead focus on the calibration of high-end six-axis IMUs (IMUs with a three-axis accelerometer and a three-axis optical angular rate sensor) used in gyrocompass systems.
- Spielvogel and Whitcomb (2018a) extend the work by Troni and Whitcomb (2019) to nine-axis IMUs. However, the work estimates magnetometer hard-iron bias only, neglecting soft-iron calibration.
- Spielvogel and Whitcomb (2020) report an observer for magnetometer hard-iron and soft-iron bias estimation in two-axis magnetometers. This observer, however, is not suitable for the full three-axis calibration of magnetometers on many robotic vehicles.

The present article reports a novel method for real-time estimation and compensation of three-axis magnetometer soft-iron and hard-iron and angular rate sensor biases utilizing biased angular rate sensor measurements. The proposed MAVBE algorithm requires smaller angular motion compared to previously reported magnetometer bias estimation methods, does not require any knowledge of the instrument's attitude, can be implemented online in real time, exhibits rapid estimate convergence, and requires only knowledge of the local magnetic field magnitude. If the local magnetic field magnitude is not known, the proposed method can still recover the direction of the magnetic field vector, which is all that is needed for accurate navigation.

1.3. Paper Outline

This article is organized as follows: Section 2 gives an overview of mathematical operators and definitions used in this article. Section 3 reports the exact deterministic process model, a discrete-time stochastic approximate process model, and an EKF formulation of the MAVBE. Section 4

discusses the evaluation methodology of the MAVBE. Section 5 reports a numerical simulation evaluation of the MAVBE approach for magnetometer and angular velocity sensor bias estimation, bias compensation, and heading estimation. Section 6 reports laboratory experimental evaluation of the MAVBE approach in full-scale UV laboratory experimental trials. Section 7 reports field experiments of the MAVBE method in full-scale AUV field experiments in the Chesapeake Bay, Maryland, USA. Section 8 summarizes and concludes.

2. Math Preliminaries

2.1. Operators

The following operators will be used in the paper.

Skew-Symmetric Operator: \mathcal{J} is a mapping $\mathbb{R}^3 \to so(3)$, such that $\forall x \in \mathbb{R}^3$,

$$\mathcal{J}(x) = \begin{bmatrix} 0 & -x_3 & x_2 \\ x_3 & 0 & -x_1 \\ -x_2 & x_1 & 0 \end{bmatrix} , \tag{1}$$

where $x = [x_1 \ x_2 \ x_3]^T$.

Jacobian Operator: **D** is a mapping $\mathbb{R}^m \to \mathbb{R}^{m \times n}$, such that for $x \in \mathbb{R}^n$ and $f : \mathbb{R}^n \to \mathbb{R}^m$, $\mathbf{D}_x[f(x)]_{\mu}$ gives the $m \times n$ Jacobian of f(x) with respect to x evaluated at μ .

Stack Operator: $(\cdot)^s$ is a mapping $\mathbb{R}^{m \times n} \to \mathbb{R}^{mn}$. For a matrix $A \in \mathbb{R}^{m \times n}$, the stack operator (Schäcke, 2013) is defined as

$$A^{s} = [a_{11} \dots a_{m1} a_{12} \dots a_{m2} \dots a_{1n} \dots a_{mn}]^{T}.$$
(2)

2.2. Kronecker Product

The Kronecker product (Loan, 2000; Schäcke, 2013) of matrix $A \in \mathbb{R}^{p \times q}$ and $B \in \mathbb{R}^{r \times s}$, denoted $A \otimes B \in \mathbb{R}^{pr \times qs}$, is defined as

$$A \otimes B = \begin{bmatrix} a_{11}B & \dots & a_{1q}B \\ \vdots & & \vdots \\ a_{p1}B & \dots & a_{pq}B \end{bmatrix}.$$

$$(3)$$

2.3. Definitions

Persistent Excitation (Narendra and Annaswamy, 1989; Sastry and Bodson, 1989): A matrix function $W: \mathbb{R}^+ \to \mathbb{R}^{m \times n}$ is persistently exciting (PE) if there exist $T, \alpha_1, \alpha_2 > 0$ such that $\forall t \geq 0$:

$$\alpha_1 I_m \ge \int_t^{t+T} \mathcal{W}(\tau) \mathcal{W}^T(\tau) \, d\tau \ge \alpha_2 I_m,\tag{4}$$

where $I_m \in \mathbb{R}^{m \times m}$ is the identity matrix.

3. Magnetometer and Angular Velocity Bias Estimator (MAVBE) Formulation

This section reports the derivation of a novel online magnetometer and angular velocity bias estimator (MAVBE) for simultaneous hard-iron and soft-iron magnetometer and angular-rate sensor bias estimation and compensation. The biases are assumed to be very slowly time varying, and hence we model them as constant terms and update the estimates continuously.

3.1. Exact System Process Model

Magnetometers (including those employed in IMUs) are subject to two primary sensor calibration errors: hard-iron and soft-iron biases. Hard-iron biases are constant magnetometer sensor bias terms due to the permanent magnetic signature of the instrument and the vehicle. Soft-iron biases are nonconstant magnetometer sensor bias terms due to the magnetic permeability of the instrument and the vehicle, and will vary with vehicle heading and attitude. For most IMU magnetometers, hard-iron biases dominate soft-iron biases.

The most commonly utilized models for three-axis magnetometer hard-iron and soft-iron bias and for three-axis angular velocity sensor bias are

$$m_m(t) = Tm_t(t) + m_b, (5)$$

$$w_m(t) = w_t(t) + w_b, (6)$$

where $m_m(t) \in \mathbb{R}^3$ and $m_t(t) \in \mathbb{R}^3$ are the noise-free measured and true magnetometer values, respectively, in the instrument frame; $T \in \mathbb{R}^{3 \times 3}$ is a positive definite symmetric (PDS) matrix due to soft-iron effects; $m_b \in \mathbb{R}^3$ is the sensor bias due to hard-iron effects; $w_m(t) \in \mathbb{R}^3$ and $w_t(t) \in \mathbb{R}^3$ are the noise-free measured and true angular velocity signals, respectively, in the instrument frame; and $w_b \in \mathbb{R}^3$ is the angular velocity bias.

The PDS matrix T is parameterized as

$$T = \begin{bmatrix} a & b & c \\ b & d & e \\ c & e & f \end{bmatrix}, \tag{7}$$

where we define $t_p \in \mathbb{R}^6$ as the vector of the six unique elements of T such that

$$t_p = \begin{bmatrix} a & b & c & d & e & f \end{bmatrix}^T. \tag{8}$$

The true magnetometer value in the north-east-down (NED) frame, ${}^w m_t \in \mathbb{R}^3$, is constant and is related to the true magnetometer value in the instrument frame by

$$^{w}m_{t} = R(t) m_{t}(t), \tag{9}$$

where $R(t) \in SO(3)$ is the time-varying rotation of the instrument frame with respect to the NED frame. Taking the time derivative of (9) yields

$$0 = \dot{R}(t) \ m_t(t) + R(t)\dot{m}_t(t). \tag{10}$$

Rearranging (10) yields

$$\dot{m}_t(t) = -\mathcal{J}(w_t(t))m_t(t),\tag{11}$$

and substituting (6) yields

$$\dot{m}_t(t) = -\mathcal{J}(w_m(t) - w_b)m_t(t). \tag{12}$$

Since the bias terms are assumed to be at most very slowly time varying, they are modeled as constants. Finally, the full state process model can be written in state space form as

$$\begin{bmatrix} \dot{m}_t(t) \\ \dot{m}_b \\ \dot{t}_p \\ \dot{w}_b \end{bmatrix} = \begin{bmatrix} -\mathcal{J}(w_m(t) - w_b)m_t(t) \\ \mathbb{O}_{3\times 1} \\ \mathbb{O}_{6\times 1} \\ \mathbb{O}_{3\times 1} \end{bmatrix}$$
(13)

$$\dot{\Phi}(t) = f(\Phi(t)), \tag{14}$$

with the measurement model

$$\begin{bmatrix}
m_m(t) \\
\|m_t(t)\|^2
\end{bmatrix} = \begin{bmatrix}
T m_t(t) + m_b \\
m_t^T(t)m_t(t)
\end{bmatrix}$$
(15)

$$z(t) = h(\Phi(t)), \tag{16}$$

where $\mathbb{O}_{m\times n}$ is a zero matrix of dimension $m\times n$, $\Phi(t)\in\mathbb{R}^{15}$ is the state vector, and $z(t)\in\mathbb{R}^4$ is the measurement. The w_b bias term is included in the state vector because we have a process model for it (bias is assumed to be constant); however, the time-varying $w_m(t)$ term was excluded from the state since its process model is unknown. It is instead considered to be an exogenous input signal. Modeling $w_m(t)$ as a exogenous input is a common approach used in magnetometer calibration (e.g., (Troni and Whitcomb, 2019; Han et al., 2017; Soken and Sakai, 2019). Note that unlike in the work by Troni and Whitcomb (2019), herein we do not assume the angular velocity signal to be already bias compensated.

As seen in (15), the measurement model requires knowledge of the magnitude of the local magnetic field vector which is available for most field vehicles via the World Magnetic Model (WMM) (NCEI Geomagnetic Modeling Team and British Geological Survey, 2019) or the International Geomagnetic Reference Field model (Thébault et al., 2015). Note that if the local magnetic field vector magnitude is unknown, by setting $||m_t(t)||^2$ to a nonzero positive constant (e.g., setting $||m_t(t)||^2 = 1$ will normalize the estimated corrected magnetic field vector to 1), the direction of the corrected magnetic field vector can still recovered, allowing accurate magnetic heading estimates.

3.2. MAVBE Process Model Linearization

The MAVBE EKF was implemented using a linear process model. The nonlinear dynamics given in (14) were linearized using an approach that follows closely that used by Webster (2010). The linearization of $f(\Phi)$ about an arbitrary operating point μ is given by

$$f(\Phi(t)) = f(\mu) + \mathbf{D}_{\Phi(t)} [f(\Phi(t))]_{\mu} (\Phi(t) - \mu) + HOT.$$
(17)

Neglecting the higher-order terms (HOT) and rearranging yields

$$f(\Phi(t)) = \underbrace{\mathbf{D}_{\Phi}[f(\Phi(t))]_{\mu}}_{A(\Phi(t))} \Phi(t) + \underbrace{f(\mu) - \mathbf{D}_{\Phi}[f(\Phi(t))]_{\mu}\mu}_{u(\Phi(t))}, \tag{18}$$

where $u(\Phi(t)) \in \mathbb{R}^{15}$ is referred to as the pseudo-control input and $A(\Phi(t)) \in \mathbb{R}^{15 \times 15}$ is the Jacobian of $f(\Phi(t))$ with respect to $\Phi(t)$ evaluated at μ . The noise-free linearized process model is given by

$$\dot{\Phi} = A(\Phi(t))\Phi(t) + u(\Phi(t)),\tag{19}$$

$$z(t) = h\left(\Phi(t)\right),\tag{20}$$

where

$$A(\Phi(t)) = \mathbf{D}_{\Phi}[f(\Phi(t))]_{\mu} \tag{21}$$

$$= \begin{bmatrix} -\mathcal{J}(w_m(t) - w_b) & \mathbb{O}_{3 \times 9} & -\mathcal{J}(m_t(t)) \\ \mathbb{O}_{12 \times 3} & \mathbb{O}_{12 \times 9} & \mathbb{O}_{12 \times 3} \end{bmatrix}_{\mu}. \tag{22}$$

3.3. MAVBE Observability

The linearized system (19)–(20) is locally observable on $[t_0, t_f]$ if and only if the observability Gramian

$$M(t_0, t_f) = \int_{t_0}^{t_f} \mathcal{H}^T(t, t_0) C^T(t) C(t) \mathcal{H}(t, t_0) dt$$
(23)

is full rank, where $\mathcal{H}(t, t_0)$ is the state transition matrix (Rugh, 1996) and C(t) is the measurement Jacobian

$$C(t) = \mathbf{D}_{\Phi(t)} [h(\Phi(t))]_{\Phi(t)}. \tag{24}$$

Through numerical studies we found that a PE $w_m(t)$ signal results in a full-rank observability Gramian and, thus, local observability of the state vector. Although it is unclear how to show this result analytically, we were able to check numerically that a variety of PE $w_m(t)$ signals result in a full-rank observability Gramian and, thus, local observability of the state vector.

3.4. MAVBE Process Model Discrete-Time Stochastic Approximation

Using the approach followed by Webster (2010), the noise-free continuous-time system (19)–(20) can be approximated as the discrete-time stochastic system

$$\Phi_k = \bar{A}_{k-1}\Phi_{k-1} + \bar{B}_{k-1}u_{k-1} + w_{k-1},\tag{25}$$

$$z_k = h\left(\Phi_k\right) + v_k,\tag{26}$$

where Φ_k is $\Phi(k)$ at time t = k, u_k is $u(\Phi(k))$, $w_k \sim \mathcal{N}(0, Q)$ is the independent zero-mean Gaussian process noise, and $v_k \sim \mathcal{N}(0, R)$ is the independent zero-mean Gaussian measurement noise. Note that we have an exact deterministic noise-free continuous-time plant model; we do not have a continuous-time noise model for plant process noise. Here we construct a discrete-time approximation of the noise-free continuous-time plant model and adopt the assumption of additive zero-mean Gaussian discrete-time process noise. The process noise for the discrete system was chosen to be a diagonal matrix for simplicity and ease of tuning.

 \bar{A}_k is related to $A(\Phi(k))$ by

$$\bar{A}_k = e^{A(\Phi_k)\tau},\tag{27}$$

where τ is the discretization time step. Similarly, \bar{B}_k can be computed as

$$\bar{B}_k = \int_0^\tau e^{A(\Phi_k)(\tau - s)} ds \tag{28a}$$

$$=e^{A(\Phi_k)\tau} \int_0^\tau e^{-A(\Phi_k)s} ds \tag{28b}$$

$$= \bar{A}_k \int_0^\tau e^{-A(\Phi_k)s} ds. \tag{28c}$$

3.5. MAVBE Extended Kalman Filter for Magnetometer Bias Estimation

The process model used to predict the state is

$$\Phi_k' = \bar{A}_{k-1}\Phi_{k-1} + \bar{B}_{k-1}u_{k-1},\tag{29}$$

and the predicted covariance matrix is

$$\Sigma_{k}' = \bar{A}_{k-1} \Sigma_{k-1} \bar{A}_{k-1}^{T} + Q, \tag{30}$$

where Q is the process noise covariance matrix (constant). The Kalman gain is given by

$$K_k = \Sigma_k' \bar{C_k}^T (\bar{C_k} \Sigma_k' \bar{C_k}^T + R)^{-1}, \tag{31}$$

where R is the measurement covariance matrix (constant), and

$$\bar{C}_k = \mathbf{D}_{\Phi}[\ h(\Phi_k)\]_{\Phi'_k} \tag{32}$$

$$= \begin{bmatrix} T & \mathbb{I}_3 & (m_t^T(k) \otimes \mathbb{I}_3) D_{t_p}[T^s] & \mathbb{O}_{3\times 3} \\ 2m_t^T(k) & \mathbb{O}_{1\times 3} & \mathbb{O}_{1\times 6} & \mathbb{O}_{1\times 3} \end{bmatrix}_{\Phi'_k},$$
(33)

where \mathbb{I}_n is the identity matrix of dimension $n \times n$.

The updated state estimate is

$$\Phi_k = \Phi_k' + K_k(z_k - \bar{C}_k \Phi_k'). \tag{34}$$

The updated covariance estimate is

$$\Sigma_k = (\mathbb{I}_{15} - K_k \bar{C}_k) \Sigma_k'. \tag{35}$$

4. MAVBE Performance Evaluation

The remainder of this paper is concerned with evaluating the proposed MAVBE presented in Section 3 in comparison to previously reported approaches to magnetometer bias estimation. We report a comparative performance analysis of the proposed MAVBE to the widely cited batch-processing TWOSTEP method reported by Alonso and Shuster (2002b). We note that Dinale (2013) provides an excellent overview of the TWOSTEP method. In particular, his Appendix C.1 provides a reference Matlab implementation of the TWOSTEP method, which proved to be very helpful to the current authors when implementing the TWOSTEP comparison.

We evaluate the performance of these approaches in the following three ways:

- 1. In Section 5, we report the evaluation of these approaches in numerical simulations in which both the true simulated bias values and the true simulated heading values are known exactly.
- 2. In Section 6, we report the evaluation of these approaches in full-scale laboratory experimental trials with a laboratory test-bed ROV in which the true sensor biases are unknown, and thus the accuracy of the estimated biases cannot be measured directly. Instead, the accuracy of the heading estimate is used as an error metric for sensor bias estimation. The heading estimate was computed using accelerometer and magnetometer signals from the MicroStrain 3DM-GX5-25 9-Axis IMU (LORD Sensing-MicroStrain, Williston, Vermont, USA) (Microstrain Inc., 2012), together with the sensor bias estimates. In the laboratory experiments, the estimated heading was compared to the ground truth heading from a high-end inertial navigation system (INS), the iXBlue PHINS III (iXBlue SAS, Saint-Germain en Laye, France), with heading accuracy of 0.05°/cos (latitude) (iXblue SAS, Saint-Germain en Laye, France, 2008; IXSEA, 2008).
- 3. In Section 7, we report the evaluation of these approaches in full-scale sea trials with the JHU Iver3 (OceanServer Technology, Inc., 2016), in which neither the true bias values nor the true heading is known. In the field experimental trials, vehicle XY navigation error is used as a proxy for the accuracy of the magnetometer calibration. The vehicle track is recalculated using Doppler dead reckoning for each magnetometer calibration method and compared to the GPS track of the vehicle. In addition to the TWOSTEP method, the proposed MAVBE is compared to L3 OceanServer's commercial solution for a calibrated magnetic compass using the OceanServer OS5000 magnetic compass (OceanServer Technology, Inc., 2015).

4.1. Attitude Calculation

The vehicle coordinates are defined such that the x axis is pointed forward on the vehicle, the y axis is pointing starboard, and the z axis down. Using this coordinate frame, the instantaneous estimated roll ϕ and pitch θ angles of the vehicle can be computed by (Troni, 2013)

$$\hat{\phi} = \operatorname{atan2}\left(-a_y, -a_z\right),\tag{36}$$

$$\hat{\theta} = \operatorname{atan2}\left(a_x, \sqrt{a_y^2 + a_z^2}\right),\tag{37}$$

where a_x, a_y, a_z are the x, y, z components, respectively, of the accelerometer signal. The calibrated magnetic field vector, $m_t(t)$, in the vehicle frame is transformed to the local level frame by the relation ${}^l m = {}^l_v R(t) m_t(t)$, where ${}^l_v R(t) \in SO(3)$ is the rotation matrix using the roll and pitch

estimates. The instantaneous estimated heading can then be computed as (Troni, 2013)

$$\hat{\gamma} = \operatorname{atan2}\left(-^{l}m_{y},^{l}m_{x}\right) - \gamma_{0},\tag{38}$$

where γ_0 is the known local magnetic variation and where ${}^l m_x, {}^l m_y, {}^l m_z$ are the x, y, z components, respectively, of the ${}^l m$ signal.

4.2. Doppler Dead Reckoning Navigation

DVLs are commonly used on UVs to measure vehicle three-axis velocity. When a DVL has bottom-lock, the instrument provides accurate measurements of the UV's three-axis velocity with respect to the fixed seafloor.

Using the roll, pitch, heading attitude of the vehicle, these velocity measurements can be transformed into world frame by (Troni, 2013)

$$^{w}v(t) = ^{w}_{v}R(t)^{v}_{i}R^{i}v(t),$$
 (39)

where ${}^{v}_{i}R$ is the constant rotation matrix from the instrument coordinate frame to the vehicle coordinate frame, ${}^{w}_{v}R(t)$ is the time-varying rotation matrix from the vehicle coordinate frame to the inertial world coordinate frame (the rotation matrix corresponding to the roll, pitch, and heading of the vehicle), ${}^{i}v(t)$ is the vehicle's velocity in the DVL instrument's coordinate frame, and ${}^{w}v(t)$ is the world frame vehicle velocity. ${}^{w}v(t)$ can then be integrated to provide the dead reckoning position estimate (Whitcomb et al., 1999)

$${}^{w}p(t) = {}^{w}p(t_0) + \int_{t_0}^{t} {}^{w}v(\tau) d\tau.$$
(40)

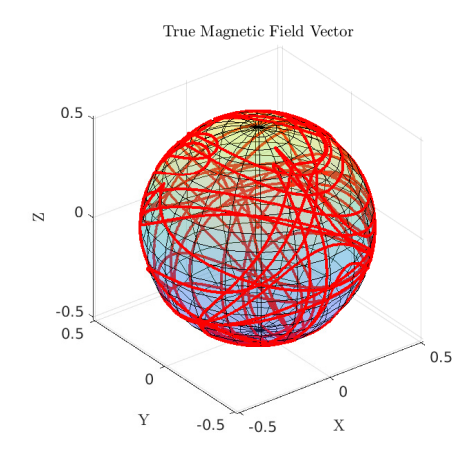
5. MAVBE Simulation Evaluation

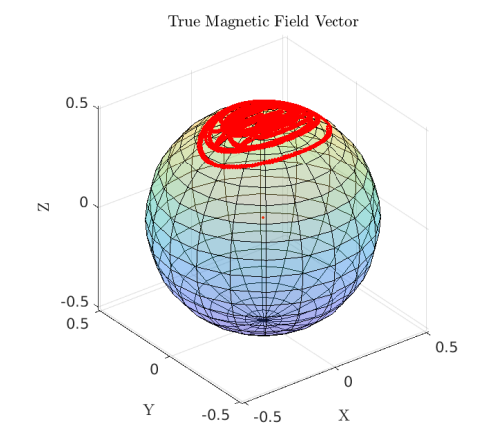
5.1. Simulation Setup

The proposed bias estimation and compensation algorithm was evaluated in a numerical simulation using Matlab. Simulated IMU sensor measurements were generated by simulating sinusoidal vehicle motions. The simulated data were generated at 20 Hz. Noise was added to these data with characteristics observed from experimental bench tests of a MicroStrain 3DM-GX5-25 (Microstrain Inc., 2012). The measured standard deviations of the simulated magnetometer and angular-rate sensors sampled at 20 Hz and the simulated "true" sensor biases used during the simulated data generation, which are realistic sensor bias values for a MicroStrain 3DM-GX5-25 as observed from bench tests, are given in Table 1.

Table 1. Simulation setup parameters.

	Sensor Noise
σ_m	$ [2 \ 2 \ 2]^T \cdot 10^{-4} \text{ G} $ $ [2.4 \ 2.4 \ 2.4]^T \cdot 10^{-4} \text{ rad/s} $
$\frac{\sigma_w}{}$	Sensor Bias
m_b w_b t_p	$[0.6 -0.7 -1]^T \cdot 10^{-1} \text{ G}$ $[-2 \ 3 \ -1]^T \cdot 10^{-3} \text{ rad/s}$ $[1.1 \ 0.1 \ 0.03 \ 0.95 \ 0.01 \ 1.2]^T$
- <u></u>	Sensor Bias Estimate Initial Values
$\hat{m}_b(t_0) \ \hat{t}_ ho(t_0) \ \hat{w}_b(t_0)$	$\begin{bmatrix} 0 \ 0 \ 0 \end{bmatrix}^T \ G$ $\begin{bmatrix} 1 \ 0 \ 0 \ 1 \ 0 \ 1 \end{bmatrix}^T$ $\begin{bmatrix} 0 \ 0 \ 0 \end{bmatrix}^T \ rad/s$





(a) Sim1: True magnetic field vector.

(b) Sim2: True magnetic field vector.

Figure 3. Simulation: The true magnetic field vectors in the instrument frame during the simulations.

Table 2. Estimated bias values for the two numerical simulations.

	m_b (G)	t_p	w _b (°/s)
True	$[0.060 \ -0.070 \ -0.100]$	[1.100 0.100 0.030 0.950 0.010 1.200]	[-0.002 0.003 -0.001]
MAVBE Sim1	[0.059 -0.070 -0.100]	[1.099 0.100 0.030 0.949 0.010 1.200]	[-0.002 0.003 -0.001]
TWOSTEP Sim1	[0.064 -0.080 -0.084]	[1.100 0.100 0.030 0.950 0.010 1.200]	N/A
MAVBE Sim2	[0.060 -0.070 -0.096]	[1.100 0.100 0.030 0.950 0.010 1.192]	[-0.002 0.003 -0.001]
TWOSTEP Sim2	[0.062 -0.075 -0.123]	[1.148 0.104 0.031 0.992 0.009 1.317]	N/A

The simulated instrument experienced smooth sinusoidal rotations. In Sim1, the instrument experiences changes in roll, pitch, and heading of $\pm 180^{\circ}$. However, in Sim2 the instrument experiences smaller angular rotations with roll and pitch magnitudes of $< 50^{\circ}$ and heading of $\pm 180^{\circ}$. Figure 3 shows the true magnetic field in the instrument frame.

The MAVBE was executed at 10 Hz, the initial conditions for the sensor biases estimates are given in Table 1, and the measurement covariance matrix, R, was populated with the square of the measured standard deviations, along the diagonal entries such that

$$R = \operatorname{diag}([4\ 4\ 4]) \cdot 10^{-8},\tag{41}$$

and a process covariance matrix, Q, that works well is

$$Q = \operatorname{diag}([1\ 1\ 1\ 1\ 1\ 1\ 1\ 1\ 1\ 1\ 1\ 1\ 0.01\ 0.01\ 0.01]) \cdot 10^{-10}. \tag{42}$$

Larger Q values resulted in quicker convergence, at the expense of more oscillatory final steady states, while lower Q values resulted in slower convergence, but a smoother final steady state. We selected Q empirically to provide a balance between convergence time and a smooth final steady state. In the future, two different process covariance matrices could be chosen for coarse and fine alignment in order to achieve fast convergence and a less oscillatory final steady state. Also, after an initial calibration, previous estimates for the sensor biases can be used as initial conditions to the MAVBE in order to greatly decrease convergence time of the proposed estimator.

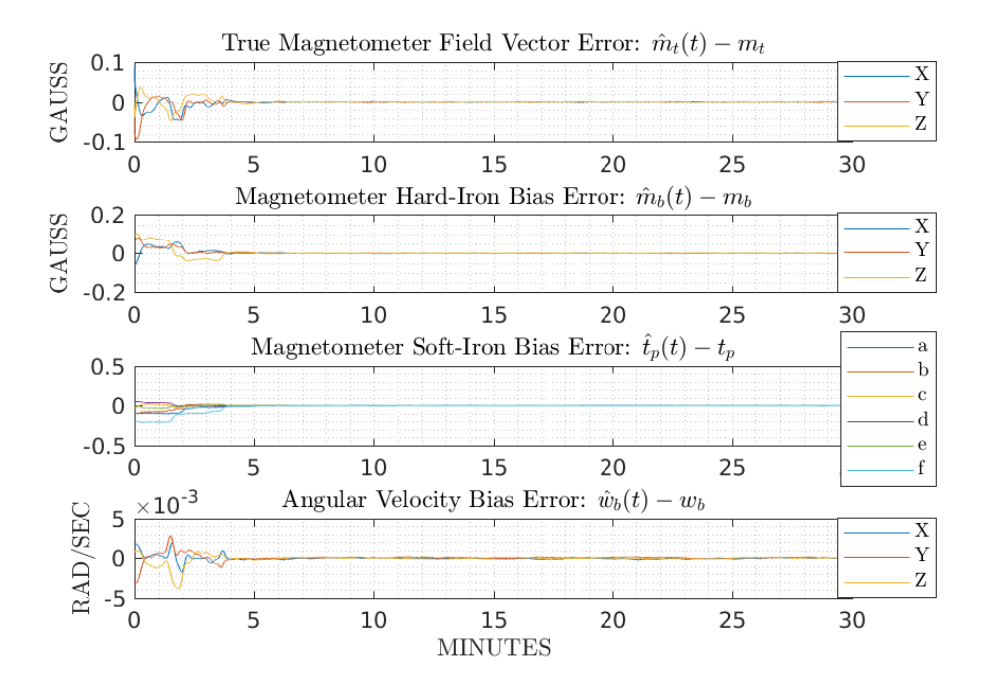


Figure 4. Simulation 1 results. MAVBE magnetometer and angular rate sensor bias estimate errors converge to zero; i.e., the estimated biases converge to their known true values.

Table 3. Comparison of heading root mean square errors (RMSEs) between the calibration methods during the numerical simulations.

Calibration Method	Sim1	Sim2	
Uncalibrated	23.35°	19.21°	
MAVBE	0.54°	0.58°	
TWOSTEP	0.61°	1.42°	

5.2. Simulation Results

Figures 4 and 5 show the evolution of the error of the estimated sensor biases for the two simulations. The simulation results show that the MAVBE can accurately estimate the true values of m_b , t_p , and w_h , and that the parameter estimates converge to the true parameter values within 5-10 minutes. The parameter convergence of the Sim1 simulation, shown in Figure 4, with very large $\pm 180^{\circ}$ excursions in heading, pitch, and roll, is about twice as fast as the parameter convergence of the Sim2 simulation, shown in Figure 5, with only $< 50^{\circ}$ excursions in pitch and roll. Since, in simulation, the true values of the biases are known, it is easy to verify that the bias estimates converge to the true bias values, and not to arbitrary incorrect values, which would generally be the case if $w_m(t)$ was not a PE signal.

Table 2 reports the biases estimated by the MAVBE and TWOSTEP methods during Sim1 and Sim2. In addition, Table 3 lists the heading errors corresponding to using the biases from Table 2 for magnetometer calibration.

In Sim1, the resulting heading RMSE of the calibrated magnetometer from the MAVBE and TWOSTEP methods was similar at 0.54° and 0.61° RMSE, respectively. In Sim1, the large angular rotations of the instrument provide rich magnetometer measurements, allowing both of the methods to find the true sensor biases. However, in Sim2 the resulting heading RMSE of the calibrated magnetometer from the MAVBE and TWOSTEP methods differs. The MAVBE method performs

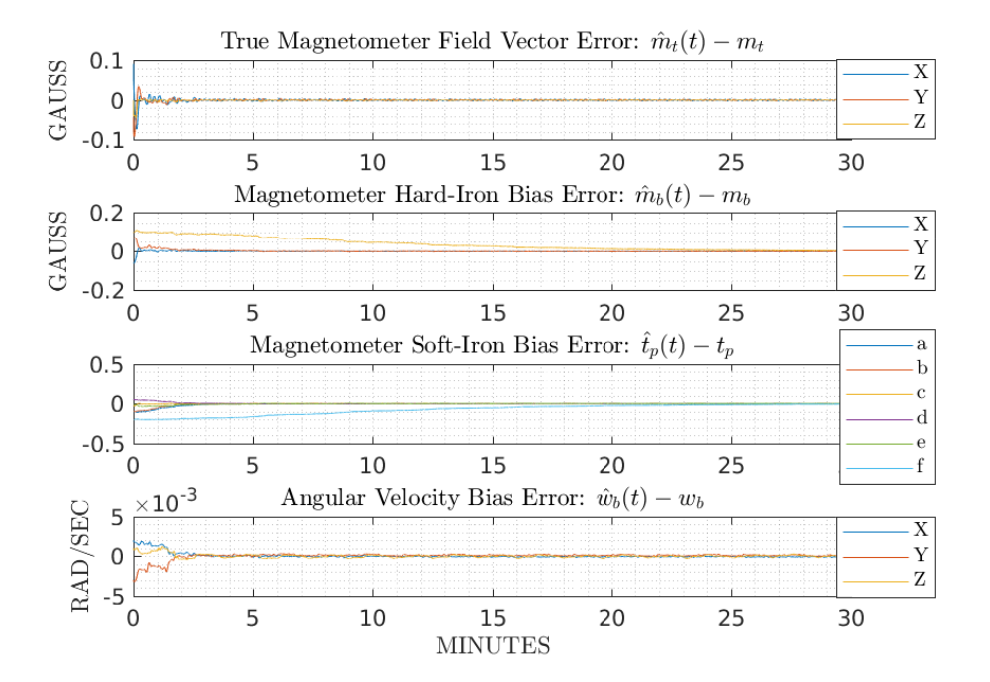


Figure 5. Simulation 2 results. MAVBE magnetometer and angular rate sensor bias estimate errors converge to zero; i.e., the estimated biases converge to their known true values.

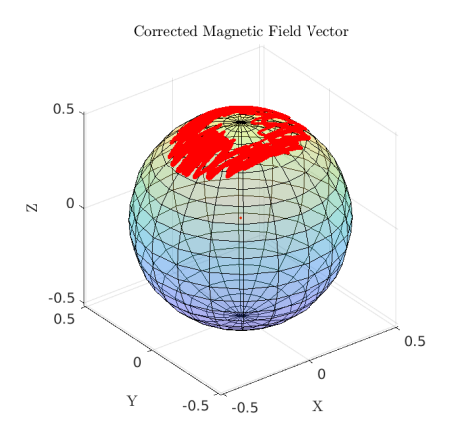
better, with a heading RMSE of 0.58°, than the TWOSTEP method with a heading RMSE of 1.42°. Since the magnetometer measurements in Sim2 are less PE than in Sim1, the use of the angular velocity measurements allows the MAVBE method to perform better than the magnetometer-only TWOSTEP method.

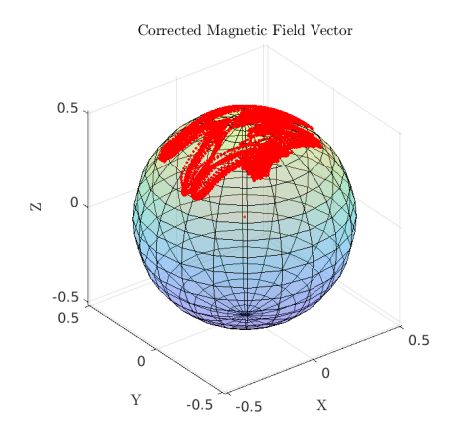
Sim2 illustrates the main benefit of the proposed MAVBE. The modest attitude motion is sufficient for the MAVBE bias estimates to converge to their true values. However, in Sim2, the TWOSTEP method is unable to estimate all of the magnetometer bias terms accurately.

The proposed MAVBE estimator's ability to converge to the proper biases while the instrument experiences modest changes in roll and pitch allows the method to be employed on large full-scale ROVs and AUVs which are typically very stable in roll and pitch and, hence, are unable to achieve larger roll and pitch changes required by many common methods like the TWOSTEP method for magnetometer calibration. An extensive investigation of the PE requirement and how to improve convergence rate would be an interesting future study, but such studies are beyond the scope of the present paper.

5.3. Batch vs Continuous Processing and Computational Complexity

The MAVBE approach can be applied continuously in real time or in post-processing. The TWOSTEP approach is applied in post-processing to a complete data set. The computational complexity of the MAVBE approach is linear in the number of instrument observations and linear in the number of process model updates; thus its computational complexity is proportional to the temporal length of a data set. The computational complexity of the iterative TWOSTEP algorithm varies both with the size of the sample data set and the number of algorithm iterations. Dinale observed that the processing time of "TWOSTEP on the other hand seems to dramatically increase the number of iterations it takes to converge once the sample size increases above 2000 samples" (Dinale, 2013).





- (a) Exp1: Corrected magnetic field vector
- (b) Exp2: Corrected magnetic field vector

Figure 6. Laboratory experiments: The corrected magnetic field vectors for Exp1 and Exp2.

6. MAVBE Laboratory Experimental Evaluation

6.1. Experimental Test Facility

Experimental trials were performed with the JHU remotely operated vehicle (ROV), equipped with a MicroStrain 3DM-GX5-25 (Microstrain Inc., 2012), in the 7.5-m-diameter, 4-m-deep freshwater test tank in the JHU hydrodynamic test facility (HTF). The ROV is a fully actuated six-DOF vehicle with six 1.5-kW DC brushless electric thrusters and employs a suite of sensors commonly employed on deep submergence underwater vehicles. This includes a high-end INS, the iXBlue PHINS III (iXBlue SAS, Saint-Germain en Laye, France) (iXblue SAS, Saint-Germain en Laye, France, 2008; IXSEA, 2008), that is used as a "ground-truth" comparison during the experimental trials. The PHINS is a high-end INS (~\$120000) with roll, pitch, and heading accuracies of 0.01°, 0.01°, and 0.05°/cos (latitude), respectively (iXblue SAS, Saint-Germain en Laye, France, 2008). Figure 1 shows the JHU ROV operating in the test tank.

6.2. Experimental Setup

The JHU ROV was commanded to execute smooth sinusoidal rotations of roughly $\pm 180^{\circ}$ in heading and $\pm 15^{\circ}$ in pitch. Two experiments were conducted at different angular velocities. In experiment 1 (Exp1), the vehicle was subject to smaller angular velocities than in experiment 2 (Exp2). Figure 6 shows the corrected magnetic field vector during the Exp1 and Exp2 experiments, and Figure 7 presents the measured angular velocities from the two laboratory experiments. IMU data were logged at 20 Hz using the MicroStrain 3DM-GX5-25. The initial conditions for the sensor bias estimates are the same as given in Table 1. The MAVBE was executed at 10 Hz, and the process and measurement covariance matrices are given by (42) and (41), respectively.

6.3. Experimental Results

The sensor bias estimates for Exp1 and Exp2 are presented in Figures 8 and 9 and the final bias estimates in Table 4. The results show that the MAVBE sensor bias estimates converge to constant values. Since the true bias values are unknown, the final bias estimates were used for calibration of the magnetometer and angular rate sensors, enabling heading error to be used as an error metric. Table 5 reports the MAVBE's and TWOSTEP's calibrated magnetometer respective heading errors. In both laboratory experiments, the heading estimates corresponding to the MAVBE calibrated magnetometer closely tracks the ground-truth value with a RMSE of roughly 1°. However, the

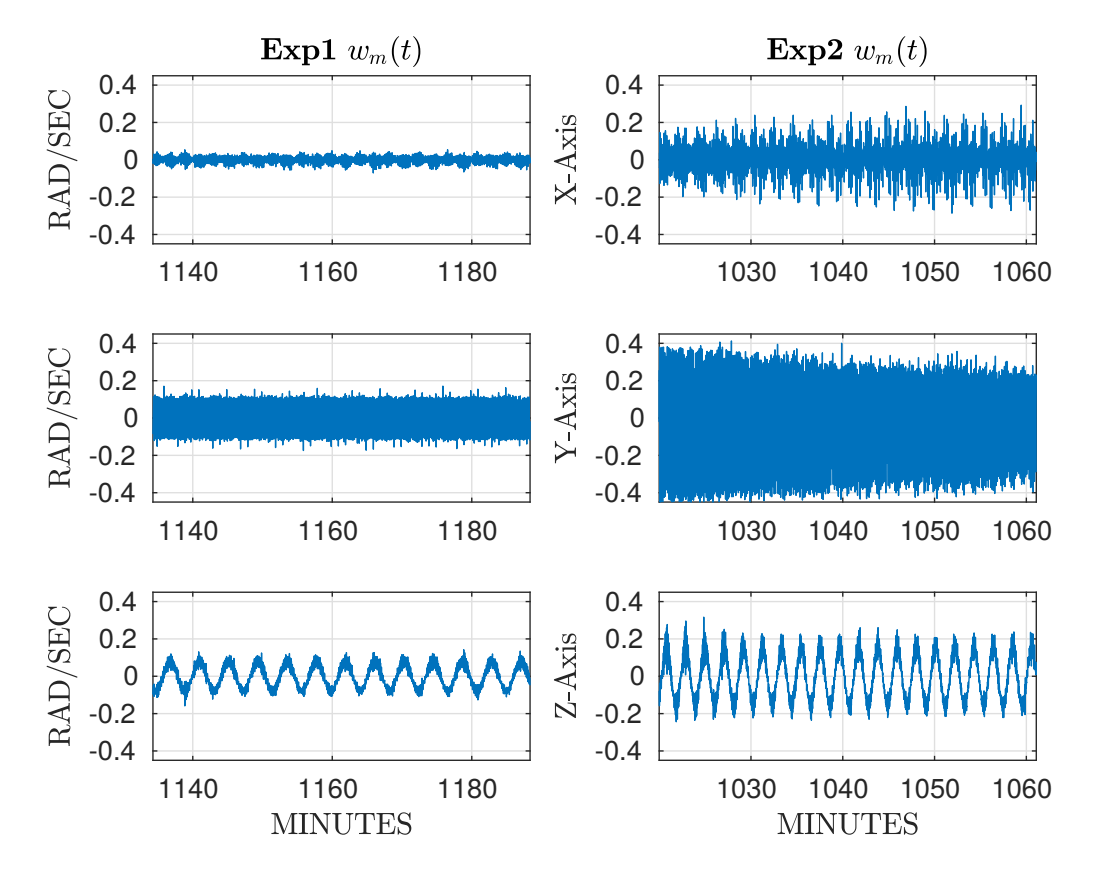


Figure 7. Laboratory experiments: Exp1 and Exp2 angular velocity measurements.

Table 4. Estimated bias values for the two laboratory experiments.

	m_b (G)	t_p	w _b (°/s)
MAVBE Exp1	[0.053 0.006 0.171]	[0.662 0.005 0.028 0.634 0.009 0.974]	[0.0006 0.0019 0.0006]
TWOSTEP Exp1	[0.123 0.002 0.874]	[0.346 0.003 0.017 0.327 0.006 0.395]	N/A
MAVBE Exp2	[0.054 0.008 0.171]	[0.681 0.009 0.031 0.645 0.007 0.990]	[0.0002 0.0018 0.0005]
TWOSTEP Exp2	[0.106 0.024 0.070]	[0.629 0.010 0.012 0.600 -0.001 1.025]	N/A

Table 5. Comparison of heading RMSEs between different calibration techniques for the two laboratory experiments.

Calibration Method	Exp1	Exp2	
Uncalibrated	23.34°	28.00°	
MAVBE	0.75°	1.12°	
TWOSTEP	2.88°	2.60°	

TWOSTEP calibrated magnetometer leads to a worse RMSE of $> 2.5^{\circ}$. The difference between the RMSE corresponding to the MAVBE and TWOSTEP calibration methods demonstrates the advantage of the MAVBE method for providing accurate magnetometer calibration on field vehicles that are unable to achieve the large roll and pitch changes required by many common methods like the TWOSTEP and ellipsoid fitting methods for magnetometer calibration.

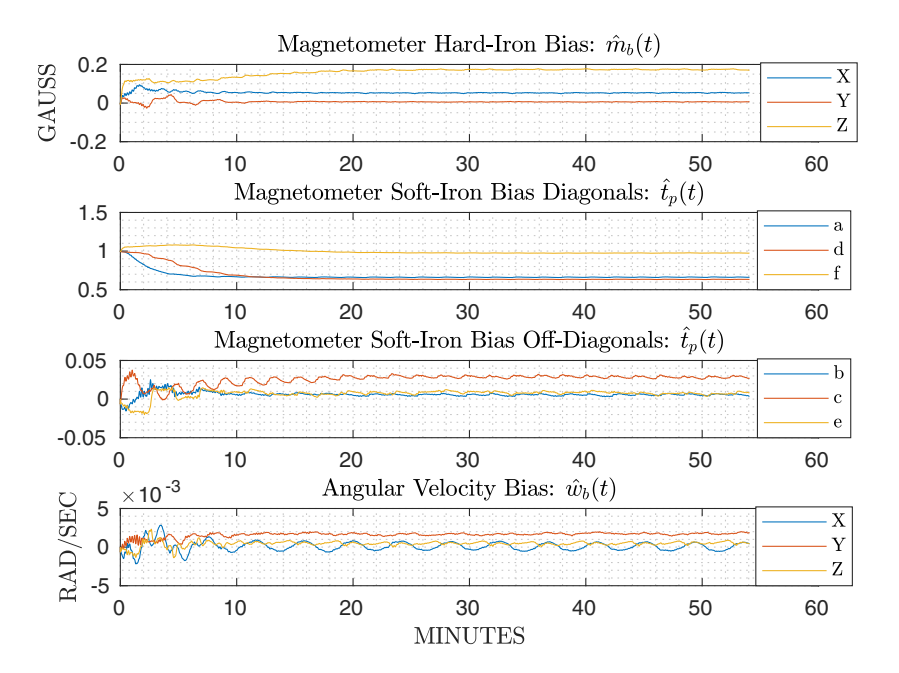


Figure 8. Experiment 1 (Exp1) results: MAVBE magnetometer and angular rate sensor bias estimates converge to constant values.

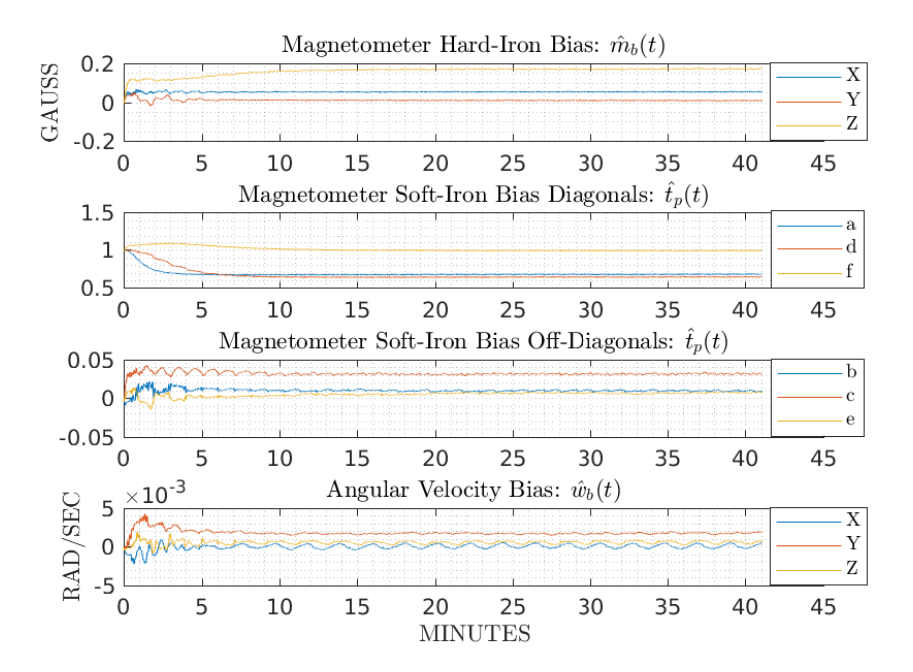


Figure 9. Experiment 2 (Exp2) results: MAVBE magnetometer and angular rate gyro bias estimates converge to constant values.

Table 6. JHU Iver3 Measurement sources, resolutions, and accuracies (Microstrain Inc., 2012; OceanServe	r
Technology, Inc., 2016, 2015; Teledyne RD Instruments, Poway, CA, USA, 2017).	

State	Source	Update Rate	Measurement Resolution	
Roll, Pitch, Heading	OceanServer OS5000 Compass Unit	1 Hz	$<0.5^{\circ}$ Heading RMSE When Level 1° Heading RMSE When $<\pm30^{\circ}$ Til-	
Linear Acceleration	Microstrain 3DM-GX5-25	20 Hz	$0.0075 \text{ m/s}^2 \text{ Std Dev}$	
Angular Velocity	Microstrain 3DM-GX5-25	20 Hz	0.00025 rad/s Std Dev	
Magnetic Field	Microstrain 3DM-GX5-25	20 Hz	0.002 gauss Std Dev	
Translational Velocity	600 kHz RDI Explorer DVL	4 Hz	0.01 m/s Std Dev	

In addition, note that in Figures 8 and 9, the sensor bias estimates in Exp2 converged faster than those in Exp1. This is due to the fact that the instrument in Exp2 experienced higher angular velocities than in Exp1 (seen in Figure 7). The increased excitement of the instrument in Exp2 leads to a faster convergence time for the sensor bias estimates than those in Exp1.

7. MAVBE Field Trial Experimental Evaluation

7.1. Test Vehicle

Experimental field trials were performed with the JHU's Iver3 AUV (L3 OceanServer, Fall River, MA, USA) (OceanServer Technology, Inc., 2016) in the Chesapeake Bay, Maryland, USA. The AUV is an underactuated AUV equipped with a 600-kHz Phased Array RDI Explorer DVL (Teledyne RD Instruments, Poway, CA, USA, 2017), a MicroStrain 3DM-GX5-25 (Microstrain Inc., 2012) IMU, and an OceanServer OS5000 (OceanServer Technology, Inc., 2015) magnetic compass. Figure 2 shows the JHU Iver3 AUV during the vehicle tests. Table 6 lists the sensors on board the JHU Iver3.

7.2. Experimental Setup

The initial conditions for the sensor bias estimates are given in Table 1, the same as in the simulations.

The 3DM-GX5-25 IMU was sampled at 20 Hz. The MAVBE was executed at 10 Hz, and the measurement covariance matrix, R, was populated with the square of the σ_m standard deviations along the diagonal entries such that R is (41), and the process covariance matrix, Q, is (42).

Before running the two field trials, a compass calibration for the Iver3's OS5000 magnetic compass (OceanServer Technology, Inc., 2015) was completed per the instructions by L3 OceanServer (OceanServer Technology, Inc., 2016). Note that the JHU Iver3 AUV has its own L3 OceanServer proprietary magnetometer calibration method for the OS5000 magnetic compass based on heading sweeps and a look-up table. This process is a two-step process involving heading sweeps on a stand and an in-water compass calibration mission. During the field trials, the proposed MAVBE method is compared not only to the TWOSTEP method (as done in the simulation and laboratory experiments), but also to OceanServer's OS5000 commercial magnetic compass.

Two field trials were conducted in Round Bay on the Chesapeake Bay, Maryland, USA. The JHU Iver3 AUV conducted two surface missions following cardinal and intercardinal heading directions. The trials were designed so that the JHU Iver3 AUV would follow track lines along cardinal and intercardinal heading directions in order to ensure that the magnetometer is fully calibrated for all heading directions. The trials were conducted on the water surface to allow for GPS to be used as a navigation ground truth and in shallow water to allow for DVL bottom-lock velocity measurements.

Table 7.	Table of	estimated	bias va	lues for	the two	field	experiments.
----------	----------	-----------	---------	----------	---------	-------	--------------

	m_b (G)	t_p	w _b (°/s)
MAVBE	[-0.084 0.149 0.0146]	$[0.986\ 0.002\ -0.001\ 0.972\ -0.002\ 0.955]$	$[0.0011 - 0.0009 \ 0.0005]$
Dive1			
TWOSTEP	$[-0.085 \ 0.1468 \ -0.005]$	[-0.009 -0.006 -0.067 -0.006 -0.071 -0.990]	N/A
Dive1	+ [0.074i 0.078i 1.088i]	+ [0.003i 0.003i 0.037i 0.003i 0.039i 0.539i]	
MAVBE	[-0.084 0.149 0.020]	[0.970 0.002 -0.002 0.966 -0.003 0.947]	[0.0012 -0.0008 0.006]
Dive2			
TWOSTEP	[0.080 0.022 0.009]	$[-0.329 \ -0.017 \ 0.067 \ -0.357 \ 0.032 \ -0.992]$	N/A
Dive2	+ [-0.057i -0.029i 0.560i]	+ [0.008i 0.004i -0.077i 0.002i -0.040i 0.754i]	·

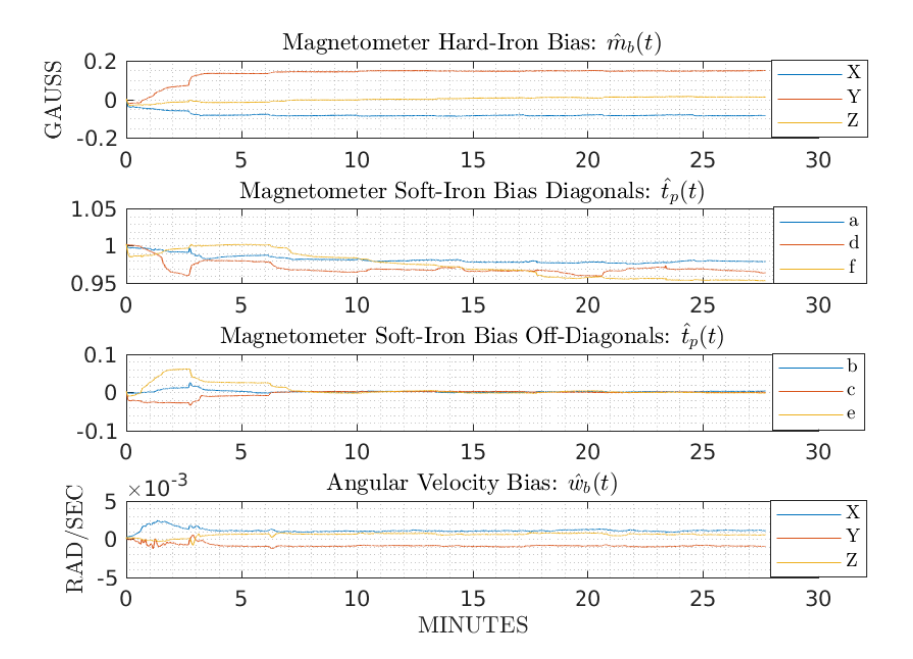


Figure 10. Dive 1 (Dive1) results: MAVBE magnetometer and angular rate sensor bias estimates converge to constant values.

Two trials were conducted ~ 4.5 hours apart (one in the morning and one in the afternoon) in order to confirm our assumption that the sensor biases were in fact slowly time varying and did not change drastically between experiments. Since the JHU Iver3 does not have a high-end INS (like used on the JHU ROV in the laboratory experiments) to compare heading estimates, navigation error is used as a proxy for the magnetometer calibration during the field trials. The recalculated dead reckoning navigation for each magnetometer calibration method is compared to the GPS track of the vehicle.

7.3. Experimental Results

The MAVBE's sensor bias estimates for Dive1 and Dive2 are presented in Figures 10 and 11 and Table 7. The results show that the MAVBE's sensor bias estimates evolve from nominal initial values to converged values within about 5–10 minutes. This also demonstrates that the motion of an actual AUV on a survey mission trajectory results in the required PE needed for convergence of the MAVBE parameter estimates. The final bias estimates were used for calibration of the magnetometer and angular rate sensor. Table 7 reports the final estimated sensor biases from Dive1 and Dive2 used

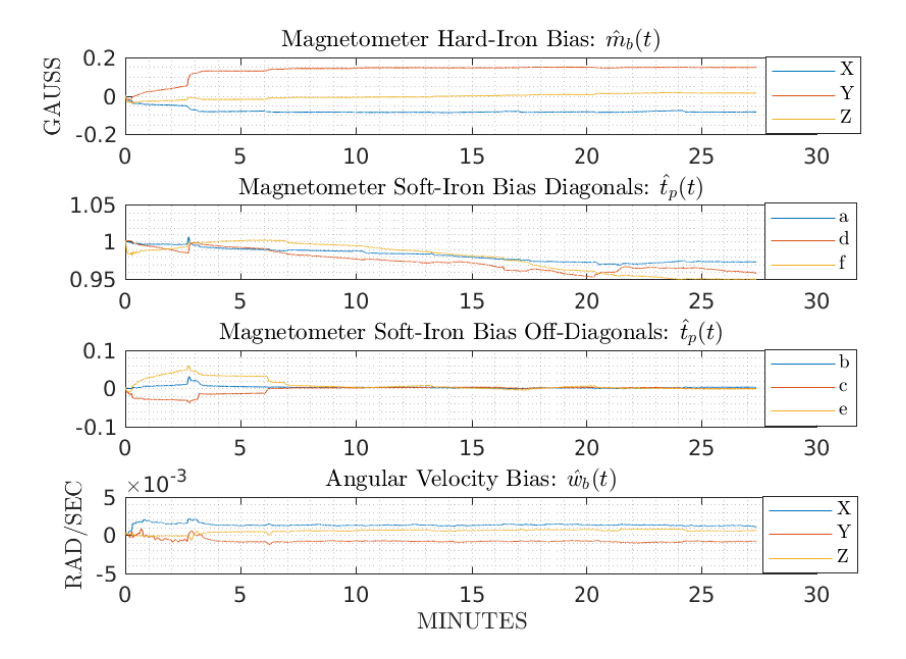


Figure 11. Dive 2 (Dive2) results: MAVBE magnetometer and angular rate sensor bias estimates converge to constant values.

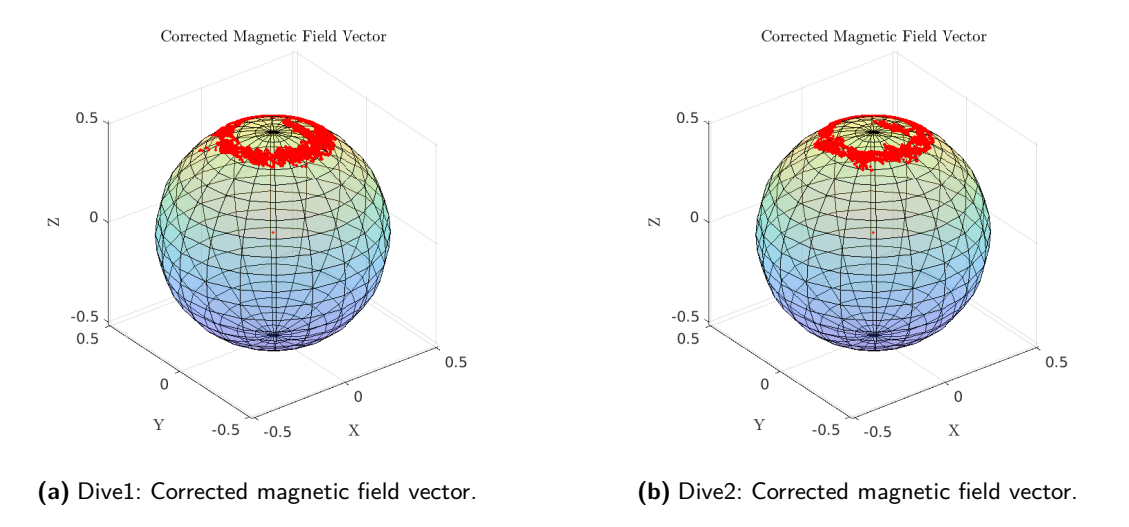


Figure 12. Field trials: The corrected magnetic field vectors for Dive1 and Dive2.

for calibration. Figure 12 shows the corrected magnetic field vectors from the two field experiments. From Figure 12, it is evident that the Iver3 AUV experienced very little excitement in roll and pitch, and hence there is not great coverage of the sphere. As discussed earlier, common methods for magnetometer calibration like the TWOSTEP and ellipsoid fitting methods require sufficient excitement of the magnetometer for their convergence to the correct sensor bias estimates. During the two field experiments, however, the AUV was stable in roll and pitch, and the TWOSTEP method was unable to accurately estimate the sensor bias. Table 7 reports the TWOSTEP estimated biases, which are clearly incorrect as they are found to be imaginary.

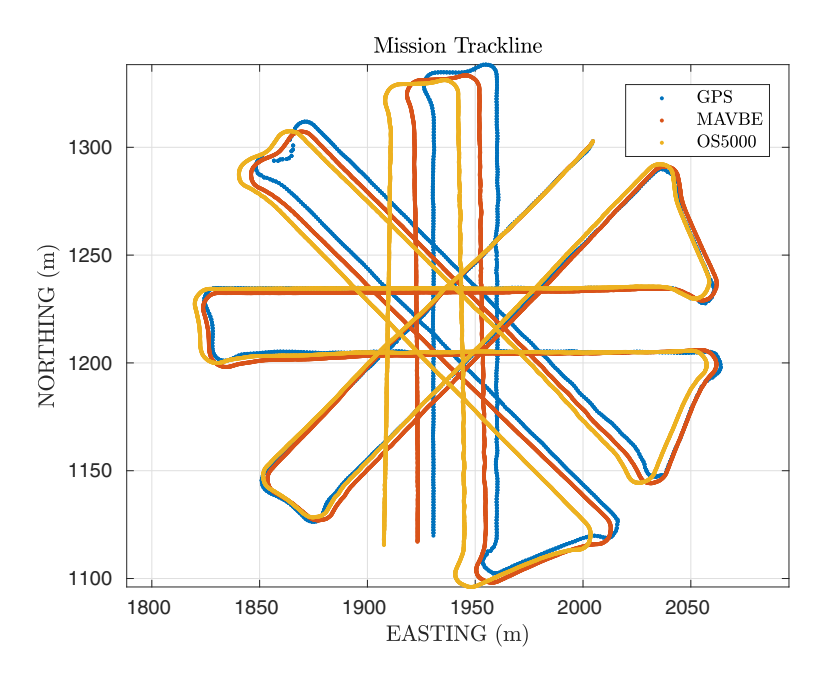


Figure 13. Dive 1 (Dive1) navigation tracks: Comparison of the Doppler dead reckoning navigation between the tracks from MAVBE compass calibration, the OS5000 calibrated compass, and the GPS ground-truth track.

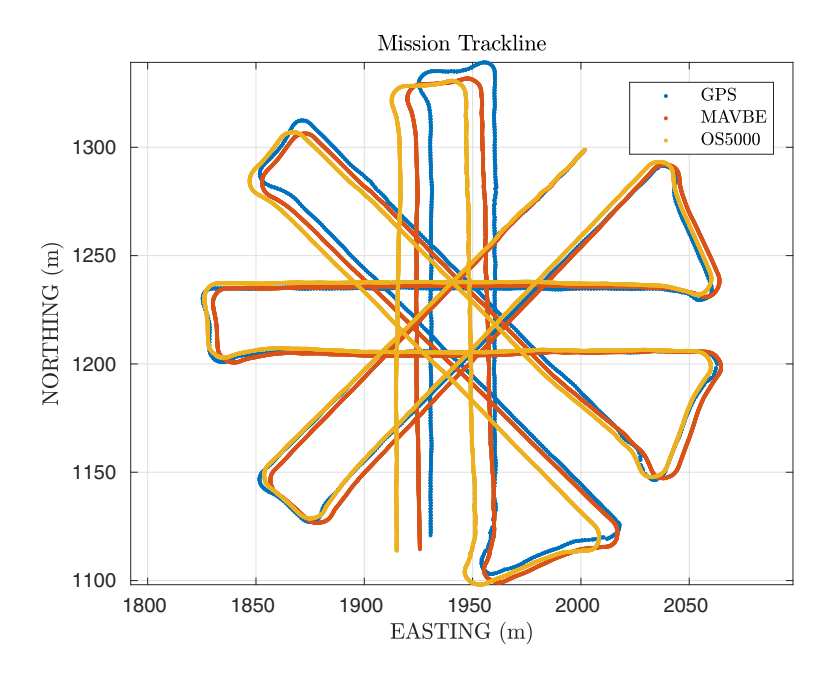


Figure 14. Dive 2 (Dive2) navigation tracks: Comparison of the Doppler dead reckoning navigation between the tracks from MAVBE compass calibration, the OS5000 calibrated compass, and the GPS ground-truth track.

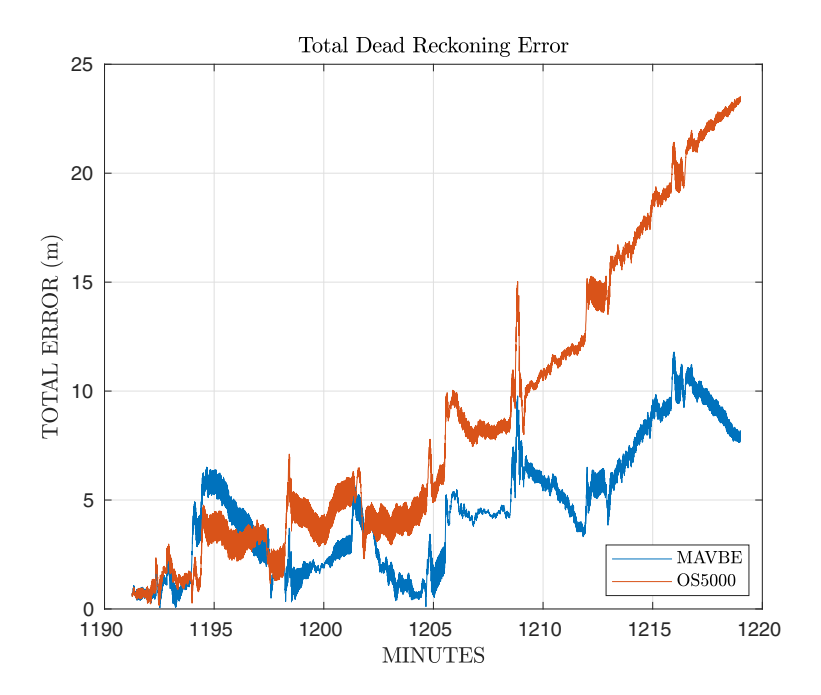


Figure 15. Dive 1 (Dive1) navigation error: Comparison of the Doppler dead reckoning navigation error of the tracks from MAVBE compass calibration and the OS5000 calibrated compass.

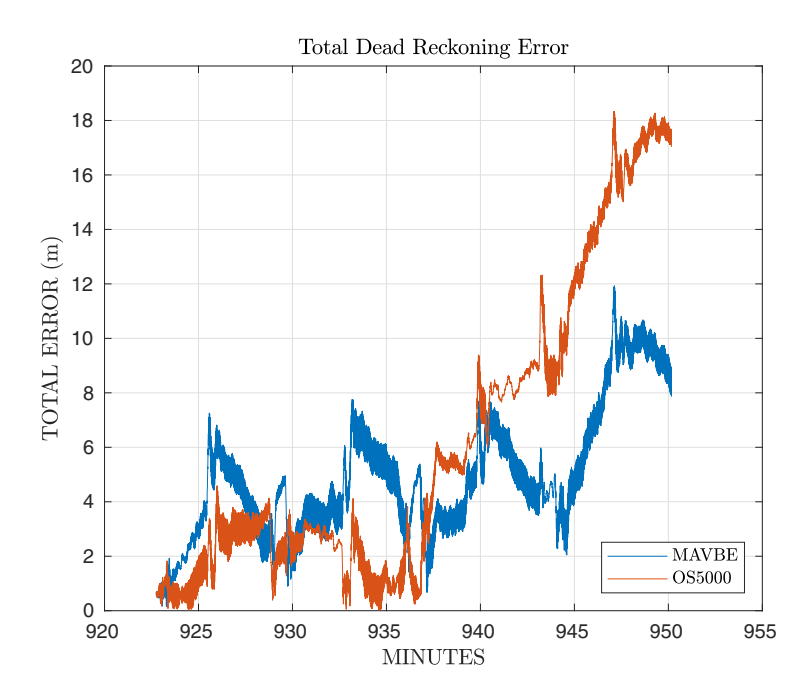


Figure 16. Dive 2 (Dive2) navigation error: Comparison of the Doppler dead reckoning navigation error of the tracks from MAVBE compass calibration and the OS5000 calibrated compass.

As reported in Table 7, the TWOSTEP algorithm failed to produce realistic bias estimates for either Dive1 or Dive2. For these dives, the TWOSTEP method produced (physically meaningless) imaginary values for the magnetometer hard-iron and soft-iron estimates. Hence, the proposed MAVBE calibration is compared to the Iver3 AUV's calibrated OS5000 compass, which relies on L3 OceanServer's proprietary magnetometer calibration method based on heading sweeps and a look-up table. In addition, since the Iver3 AUV does not have a high-end INS to provide heading as a comparison to the calibrated magnetometer heading, Doppler navigation error is used as an error metric.

Figures 13 and 14 show the MAVBE and OS5000 calibrated magnetic compass navigation tracks in comparison with the GPS ground-truth track, and Figures 15 and 16 show the respective two-norm error of the navigation tracks. From Figures 15 and 16, we see that the MAVBE calibrated compass leads to more accurate Doppler dead reckoning navigation than the industry standard provided by L3 OceanServer's calibrated OS5000 magnetic compass. The navigation track error for the Dive1 and Dive2 field experiments demonstrates that the MAVBE calibrated MicroStrain 3DM-GX5-25 provides improved performance over the calibrated OS5000 compass. In addition, the field experiments demonstrate the ability of the MAVBE method to properly calibrate magnetometers on robotic vehicles which are stable in roll and pitch and, in consequence, experience only modest excursions in roll and pitch. This is in contrast to the TWOSTEP method, which is unable to estimate the magnetometer hard-iron and soft-iron sensor bias during the field trials.

8. Conclusion

This paper reports a novel method for online, real-time estimation of hard-iron and soft-iron magnetometer biases and angular rate sensor biases in inertial measurement units (IMUs) for use in attitude and heading reference systems (AHRSs). AHRSs commonly use bias-compensated magnetometer measurements to estimate heading. By utilizing angular rate sensor measurements, smaller angular rotations of the instrument (in comparison to previously reported methods for magnetometer calibration) are required for accurate compensation of magnetometer and angular velocity sensor biases. Since the proposed estimator works with smaller changes in roll and pitch than previously reported methods, it can be implemented on real full-scale ROVs to provide online estimates of magnetometer sensor biases to allow real-time bias compensation for these sensors.

Oceanographic underwater vehicles (UVs) and surface vehicles, which are commonly passively stable in roll and pitch, are unable to achieve the roll and pitch required for the common magnetometer calibration methods like the TWOSTEP and ellipsoid fitting methods. The simulations, laboratory experiments, and field trials show that the proposed MAVBE magnetometer calibration method provides improved performance over common methods like the TWOSTEP method and the OceanServer Iver3 AUV commercial solution. The TWOSTEP method was unable to estimate the magnetometer sensor biases during the field experiments due to the limited motion in roll and pitch. The ability of the proposed MAVBE method to accurately estimate magnetometer biases when there is limited excitation of the magnetometer signal illustrates the advantage of the proposed calibration method over common calibration methods like the TWOSTEP and ellipsoid fitting methods, which fail when there is low coverage of the magnetometer on the sphere.

As demonstrated in the field experiments, the proposed method leads to improved position estimation of the Iver3 AUV over the TWOSTEP calibrated magnetometer and the calibrated OceanServer OS5000 magnetic compass.

In future studies, the authors hope to improve the convergence time of the estimator by developing coarse and fine alignment protocols. Different values for the process covariance matrix, Q, could be chosen during the coarse and fine alignment to enable both a fast convergence of the sensor biases and a smooth final steady state.

Acknowledgments

We gratefully acknowledge the support of the National Science Foundation under NSF awards OCE-1435818 and IIS-1909182. In addition, the authors acknowledge the masters thesis by Dinale (2013) which provides a clear derivation and well-documented reference source code for the TWOSTEP method originally reported by Alonso and Shuster (2002a).

ORCID

```
Andrew R. Spielvogel https://orcid.org/0000-0001-6214-9992 Abhimanyu S. Shah https://orcid.org/0000-0003-1981-5907 Louis L. Whitcomb https://orcid.org/0000-0003-2398-1000
```

References

- Alonso, R. and Shuster, M. D. (2002a). TWOSTEP: A fast robust algorithm for attitude-independent magnetometer-bias determination. *Journal of the Astronautical Sciences*, 50(4):433–452.
- Alonso, R. and Shuster, M. D. (2002b). Complete linear attitude-independent magnetometer calibration. Journal of the Astronautical Sciences, 50(4):477–490.
- Ammann, N., Derksen, A., and Heck, C. (2015). A novel magnetometer-accelerometer calibration based on a least squares approach. In 2015 International Conference on Unmanned Aircraft Systems (ICUAS), pages 577–585.
- Barfoot, T. D. (2017). State estimation for robotics. Cambridge University Press.
- Batista, P., Silvestre, C., Oliveira, P., and Cardeira, B. (2011). Accelerometer calibration and dynamic bias and gravity estimation: Analysis, design, and experimental evaluation. *IEEE Transactions on Control Systems Technology*, 19(5):1128–1137.
- Bronner, A., Munschy, M., Sauter, D., Carlut, J., Searle, R., and Maineult, A. (2013). Deep-tow 3C magnetic measurement: Solutions for calibration and interpretation. *Geophysics*, 78(3):J15–J23.
- Bry, A., Bachrach, A., and Roy, N. (2012). State estimation for aggressive flight in GPS-denied environments using onboard sensing. In 2012 IEEE International Conference on Robotics and Automation, pages 1–8. IEEE.
- Clegg, D. and Peterson, M. (2003). User operational evaluation system of unmanned underwater vehicles for very shallow water mine countermeasures. In *OCEANS* 2003, volume 3, pages 1417–1423.
- Clem, T. R., Sternlicht, D. D., Fernandez, J. E., Prater, J. L., Holtzapple, R., Gibson, R. P., Klose, J. P., and Marston, T. M. (2012). Demonstration of advanced sensors for underwater unexploded ordnance (UXO) detection. In OCEANS 2012, pages 1–4.
- Corke, P., Detweiler, C., Dunbabin, M., Hamilton, M., Rus, D., and Vasilescu, I. (2007). Experiments with underwater robot localization and tracking. In Proceedings of the 2007 IEEE International Conference on Robotics and Automation, pages 4556–4561. IEEE.
- Crassidis, J. L., Lai, K.-L., and Harman, R. R. (2005). Real-time attitude-independent three-axis magnetometer calibration. *Journal of Guidance, Control, and Dynamics*, 28(1):115–120.
- Crassidis, J. L., Markley, F. L., and Cheng, Y. (2007). Survey of nonlinear attitude estimation methods. Journal of Guidance, Control, and Dynamics, 30(1):12–28.
- Dinale, J. P. (2013). Magnetic test facility sensor and coil calibrations. Master's thesis, University of Adelaide, School of Electrical and Electronic Engineering.
- Dunbabin, M., Roberts, J., Usher, K., Winstanley, G., and Corke, P. (2005). A hybrid AUV design for shallow water reef navigation. In *Proceedings of the 2005 IEEE International Conference on Robotics and Automation*, pages 2105–2110. IEEE.
- Fang, J., Sun, H., Cao, J., Zhang, X., and Tao, Y. (2011). A novel calibration method of magnetic compass based on ellipsoid fitting. *IEEE Transactions on Instrumentation and Measurement*, 60(6):2053–2061.
- Fedele, G., D'Alfonso, L., and D'Aquila, G. (2018). Magnetometer bias finite-time estimation using gyroscope data. *IEEE Transactions on Aerospace and Electronic Systems*, 54(6):2926–2936.
- Foster, C. C. and Elkaim, G. H. (2008). Extension of a two-step calibration methodology to include nonorthogonal sensor axes. *IEEE Transactions on Aerospace and Electronic Systems*, 44(3):1070–1078.

- Guo, P., Qiu, H., Yang, Y., and Ren, Z. (2008). The soft iron and hard iron calibration method using extended Kalman filter for attitude and heading reference system. In *Position, Location and Navigation Symposium, 2008 IEEE/ION*, pages 1167–1174. IEEE.
- Hamel, T. and Mahony, R. (2006). Attitude estimation on SO(3) based on direct inertial measurements. In 2006 IEEE International Conference on Robotics and Automation (ICRA), pages 2170–2175. IEEE.
- Han, K., Han, H., Wang, Z., and Xu, F. (2017). Extended Kalman filter-based gyroscope-aided magnetometer calibration for consumer electronic devices. *IEEE Sensors Journal*, 17(1):63–71.
- Honsho, C., Ura, T., and Kim, K. (2013). Deep-sea magnetic vector anomalies over the Hakurei hydrothermal field and the Bayonnaise knoll caldera, Izu-Ogasawara arc, Japan. Journal of Geophysical Research: Solid Earth, 118(10):5147–5164.
- iXblue SAS, Saint-Germain en Laye, France (2008). iXSEA PHINS INS datasheet.
- IXSEA (2008). PHINS III User Guide. IXSEA, MU-PHINSIII-006 B edition.
- Kinsey, J. C. and Whitcomb, L. L. (2004). Preliminary field experience with the DVLNAV integrated navigation system for oceanographic submersibles. *Control Engineering Practice*, 12(12):1541–1549.
- Kok, M., Hol, J. D., Schön, T. B., Gustafsson, F., and Luinge, H. (2012). Calibration of a magnetometer in combination with inertial sensors. In 2012 15th International Conference on Information Fusion (FUSION), pages 787–793. IEEE.
- Li, X. and Li, Z. (2012). A new calibration method for tri-axial field sensors in strap-down navigation systems. *Measurement Science and Technology*, 23(10):105105.
- Loan, C. F. (2000). The ubiquitous Kronecker product. Journal of Computational and Applied Mathematics, 123(1):85–100. Numerical Analysis 2000. Vol. III: Linear Algebra.
- Mahony, R., Hamel, T., and Pflimlin, J. M. (2008). Nonlinear complementary filters on the special orthogonal group. *IEEE Transactions on Automatic Control*, 53(5):1203–1218.
- Mahony, R., Kumar, V., and Corke, P. (2012). Multirotor aerial vehicles: Modeling, estimation, and control of quadrotor. *IEEE Robotics and Automation Magazine*, 19(3):20–32.
- Metni, N., Pflimlin, J. M., Hamel, T., and Souéres, P. (2005). Attitude and gyro bias estimation for a flying UAV. In 2005 IEEE/RSJ International Conference on Intelligent Robots and Systems (IROS), pages 1114–1120.
- Metni, N., Pflimlin, J.-M., Hamel, T., and Souéres, P. (2006). Attitude and gyro bias estimation for a VTOL UAV. Control Engineering Practice, 14(12):1511–1520.
- Microstrain Inc. (2012). 3DM-GX3-25 Miniature Attitude Heading Reference System datasheet. Technical Report P/N 8400-0033 rev. 002, Microstrain Inc., Williston, VT.
- Narendra, K. S. and Annaswamy, A. M. (1989). Stable Adaptive Systems. Prentice-Hall, Upper Saddle River, NJ.
- NCEI Geomagnetic Modeling Team and British Geological Survey (2019). World Magnetic Model 2020. National Centers for Environmental Information.
- OceanServer Technology, Inc. (2015). Digital Compass Users Guide, OS5000 Series. OceanServer, Rev. 5.0 edition.
- OceanServer Technology, Inc. (2016). AUV Operating Guide. OceanServer, Rev. 5.0 edition.
- Ousaloo, H. S., Sharifi, G., Mahdian, J., and Nodeh, M. T. (2017). Complete calibration of three-axis strapdown magnetometer in mounting frame. *IEEE Sensors Journal*, 17(23):7886–7893.
- Packard, G. E., Kukulya, A., Austin, T., Dennett, M., Littlefield, R., Packard, G., Purcell, M., Stokey, R., and Skomal, G. (2013). Continuous autonomous tracking and imaging of white sharks and basking sharks using a REMUS-100 AUV. In 2013 OCEANS—San Diego, pages 1–5.
- Papafotis, K. and Sotiriadis, P. P. (2019). Computationally efficient calibration algorithm for three-axis accelerometer and magnetometer. In 2019 8th International Conference on Modern Circuits and Systems Technologies (MOCAST), pages 1–4.
- Rugh, W. J. (1996). Linear System Theory (2nd Ed.). Prentice-Hall, Upper Saddle River, NJ.
- Sastry, S. and Bodson, M. (1989). Adaptive Control: Stability, Convergence and Robustness. Prentice-Hall, Upper Saddle River, NJ.
- Scaramuzza, D., Achtelik, M. C., Doitsidis, L., Fraundorfer, F., Kosmatopoulos, E., Martinelli, A., Achtelik, M. W., Chli, M., Chatzichristofis, S., Kneip, L., Gurdan, D., Heng, L., Lee, G. H., Lynen, S., Meier, L., Pollefeys, M., Renzaglia, A., Siegwart, R., Stumpf, J. C., Tanskanen, P., Troiani, C., and Weiss, S. (2014). Vision-controlled micro flying robots: From system design to autonomous navigation and mapping in GPS-denied environments. *IEEE Robotics & Automation Magazine*, 21(3):26–40.

- Schäcke, K. (2013). On the Kronecker product. Master's thesis, University of Waterloo, Mathematics Department.
- Soken, H. E. and Sakai, S. (2019). TRIAD+filtering approach for complete magnetometer calibration. In 2019 9th International Conference on Recent Advances in Space Technologies (RAST), pages 703–708.
- Spielvogel, A. R. and Whitcomb, L. L. (2018a). Adaptive sensor bias estimation in nine degree of freedom inertial measurement units: Theory and preliminary evaluation. In 2018 IEEE/RSJ International Conference on Intelligent Robots and Systems (IROS), pages 5555–5561.
- Spielvogel, A. R. and Whitcomb, L. L. (2018b). Adaptive bias and attitude observer on the special orthogonal group for true-north gyrocompass systems: Theory and preliminary results. In *Proceedings of Robotics: Science and Systems*, Pittsburgh, PA.
- Spielvogel, A. R. and Whitcomb, L. L. (2019). Adaptive bias and attitude observer on the special orthogonal group for true-north gyrocompass systems: Theory and preliminary results. *International Journal of Robotics Research*, 39(2–3):321–338.
- Spielvogel, A. R. and Whitcomb, L. L. (2020). A stable adaptive observer for hard-iron and soft-iron bias calibration and compensation for two-axis magnetometers: Theory and experimental evaluation. *IEEE Robotics and Automation Letters*, 5(2):1295–1302.
- Steele, E., Boyd, T., Inall, M., Dumont, E., and Griffiths, C. (2012). Cooling of the West Spitsbergen Current: AUV-based turbulence measurements west of Svalbard. In 2012 IEEE/OES Autonomous Underwater Vehicles (AUV), pages 1–7.
- Teledyne RD Instruments (2017). Teledyne RD Instruments Explorer Doppler Velocity Log (DVL) Datasheet, Poway, CA.
- Thébault, E., Finlay, C. C., Beggan, C. D., Alken, P., Aubert, J., Barrois, O., Bertrand, F., Bondar, T., Boness, A., Brocco, L., Canet, E., Chambodut, A., Chulliat, A., Coïsson, P., Civet, F., Du, A., Fournier, A., Fratter, I., Gillet, N., Hamilton, B., Hamoudi, M., Hulot, G., Jager, T., Korte, M., Kuang, W., Lalanne, X., Langlais, B., Léger, J.-M., Lesur, V., Lowes, F. J., Macmillan, S., Mand ea, M., Manoj, C., Maus, S., Olsen, N., Petrov, V., Ridley, V., Rother, M., Sabaka, T. J., Saturnino, D., Schachtschneider, R., Sirol, O., Tangborn, A., Thomson, A., Tøffner-Clausen, L., Vigneron, P., Wardinski, I., and Zvereva, T. (2015). International Geomagnetic Reference Field: The 12th generation. Earth, Planets, and Space, 67:79.
- Troni, G. (2013). Advances in precision navigation of underwater vehicles. PhD thesis, Johns Hopkins University, Department of Mechanical Engineering.
- Troni, G. and Whitcomb, L. L. (2019). Field sensor bias calibration with angular-rate sensors: Theory and experimental evaluation with application to magnetometer calibration. *IEEE/ASME Transactions on Mechatronics*, 24(4):1698–1710.
- Vasconcelos, J. F., Cardeira, B., Silvestre, C., Oliveira, P., and Batista, P. (2011). Discrete-time complementary filters for attitude and position estimation: Design, analysis and experimental validation. *IEEE Transactions on Control Systems Technology*, 19(1):181–198.
- Vasconcelos, J. F., Elkaim, G., Silvestre, C., Oliveira, P., and Cardeira, B. (2011). Geometric approach to strapdown magnetometer calibration in sensor frame. *IEEE Transactions on Aerospace and Electronic* Systems, 47(2):1293–1306.
- Webster, S. (2010). Decentralized Single-Beacon Acoustic Navigation: Combined Communication and Navigation for Underwater Vehicles. PhD thesis, Johns Hopkins University, Department of Mechanical Engineering.
- Whitcomb, L., Yoerger, D., and Singh, H. (1999). Advances in Doppler-based navigation of underwater robotic vehicles. In 1999 IEEE International Conference on Robotics and Automation (ICRA), volume 1, pages 399–406.
- Wu, J. (2019). Real-time magnetometer disturbance estimation via online nonlinear programming. IEEE Sensors Journal, 19(12):4405–4411.
- Wu, T. H., Kaufman, E., and Lee, T. (2015). Globally asymptotically stable attitude observer on SO(3). In 2015 54th IEEE Conference on Decision and Control (CDC), pages 2164–2168.
- Wu, Y., Zou, D., Liu, P., and Yu, W. (2018). Dynamic magnetometer calibration and alignment to inertial sensors by Kalman filtering. *IEEE Transactions on Control Systems Technology*, 26(2):716–723.
- Wu, Z., Wu, Y., Hu, X., and Wu, M. (2013). Calibration of three-axis magnetometer using stretching particle swarm optimization algorithm. *IEEE Transactions on Instrumentation and Measurement*, 62(2):281–292.
- Zhou, M., Bachmayer, R., and de Young, B. (2014). Working towards seafloor and underwater iceberg mapping with a Slocum glider. In 2014 IEEE/OES Autonomous Underwater Vehicles (AUV), pages 1–5.

Zhu, M., Wu, Y., and Yu, W. (2019). An efficient method for gyroscope-aided full magnetometer calibration. $IEEE\ Sensors\ Journal,\ 19(15):6355-6361.$

How to cite this article: Spielvogel, A. R., Shah, A. S., & Whitcomb, L. L. (2022). Online three-axis magnetometer hard-iron and soft-iron bias and angular velocity sensor bias estimation using angular velocity sensors for improved dynamic heading accuracy. *Field Robotics*, *2*, 1001–1027.

Publisher's Note: Field Robotics does not accept any legal responsibility for errors, omissions or claims and does not provide any warranty, express or implied, with respect to information published in this article.